Human Molecular Genetics, 2021, Vol. 00, No. 00 1–10

doi: 10.1093/hmg/ddab103
Advance Access Publication Date: 15 April 2021
General Article

GENERAL ARTICLE

Snord116 Post-transcriptionally Increases Nhlh2 mRNA Stability: Implications for Human Prader-Willi Syndrome

Matthew A. Kocher[1], Fenix W. Huang[2], Erin Le[3] and Deborah J. Good[1,3,*]

[1]Translational Biology, Medicine and Health Graduate Program, 1 Riverside Circle, Virginia Tech, Roanoke, VA 24016, [2]Biocomplexity Institute & Initiative, University of Virginia, 995 Research Park Blvd, Town Center III, 4th Floor, Charlottesville, VA 22911 and [3]Department of Human Nutrition, Foods, and Exercise, 1981 Kraft Drive (0913), Integrated Life Sciences Building, Virginia Tech, Blacksburg, VA 24060

*To whom correspondence should be addressed. Email: goodd@vt.edu.

Abstract

The smallest genomic region causing Prader-Willi Syndrome (PWS) deletes the non-coding RNA *SNORD116* cluster; however, the function of *SNORD116* remains a mystery. Previous work in the field revealed the tantalizing possibility that expression of *NHLH2*, a gene previously implicated in both obesity and hypogonadism, was downregulated in PWS patients and differentiated stem cells. *In silico* RNA: RNA modeling identified several potential interaction domains between *SNORD116* and *NHLH2* mRNA. One of these interaction domains was highly conserved in most vertebrate *NHLH2* mRNAs examined. A construct containing the *Nhlh2* mRNA, including its 3'-UTR, linked to a c-myc tag was transfected into a hypothalamic neuron cell line in the presence and absence of exogenously-expressed *Snord116*. *Nhlh2* mRNA expression was upregulated in the presence of *Snord116* dependent on the length and type of 3'UTR used on the construct. Furthermore, use of actinomycin D to stop new transcription in N29/2 cells demonstrated that the upregulation occurred through increased stability of the *Nhlh2* mRNA in the 45 minutes immediately following transcription. *In silico* modeling also revealed that a single nucleotide variant (SNV) in the *NHLH2* mRNA could reduce the predicted interaction strength of the *NHLH2*:*SNORD116* diad. Indeed, use of an *Nhlh2* mRNA construct containing this SNV significantly reduces the ability of *Snord116* to increase *Nhlh2* mRNA levels. For the first time, these data identify a motif and mechanism for SNORD116-mediated regulation of *NHLH2*, clarifying the mechanism by which deletion of the *SNORD116* snoRNAs locus leads to PWS phenotypes.

Introduction

Prader-Willi Syndrome (PWS) is a devastating human genetic condition, affecting up to 1 in 10 000 live births. Affected infants present with hypotonia, as well as weak suckling and failure to thrive (1). Adolescents are hypogonadal and males show cryptorchidism, with hypogonadotropic hypogonadism at puberty (1). Hyperphagia typically begins around age 2 years (1), and results in morbid obesity in adulthood unless drastic calorie limitation is initiated.

PWS is most often due to a de novo paternal deletion of the chromosome 15q11-q13 region (at least 60% of cases) (1). The paternally-inherited 15q deletion minimally contains the *SNORD116* locus, (a group of 30 small nucleolar RNAs 'snoRNAs'), and the *IPW* gene (2). The *SNORD116* snoRNAs are 'orphan' snoRNAs meaning that they have no predicted RNA targets.

Received: January 16, 2021. **Revised:** March 31, 2021. **Accepted:** April 1, 2021

A significant gap in knowledge exists in our understanding of how deletion of this region of 15q leads to the complex phenotypes of PWS. A hint about this came in late 2016 when Burnett and colleagues showed two mRNAs—*NHLH2* and *PCSK1* were downregulated in human PWS induced pluripotent stem cell (iPSC)-derived neurons, and in the *Snord116*$^{m+/p-}$ mouse—a model animal for PWS (3). As noted in their paper, targeted deletion of *Nhlh2* (N2KO) in mice results in phenotypes that overlap that of human PWS, and the *Snord116*$^{m+/p-}$ mouse (3).

N2KO mice show an initial delay in total body weight until about 7 weeks of age in males, and then a later onset obesity, significant in both sexes by around 13 weeks of age (4). Total body fat in the females becomes significantly higher than age-matched wild-type females in the 13–19 week ages, while in males, body fat levels are significantly higher in animals older than 20 weeks old (4). Both of these phenotypes are similar in developmental stages to PWS patients. Likewise, N2KO mice demonstrate male cryptorchidism, with hypogonadotropic hypogonadism in males and females at puberty (5,6). Low physical activity levels are characteristic of both N2KO mice (4) and PWS patients—the latter showing low infantile movement (1) as well as overall physical activity levels and response to exercise (7). Both N2KO mice (KJ/hour, in preparation) and PWS patients (Kcal/day) (8) demonstrate low energy expenditure levels, contributing to overall lower metabolism levels for both the model organism and the human counterparts.

Nhlh2 is a neuronal basic helix–loop–helix transcription factor that controls genes within the leptin-melanocortin pathway (9), including prohormone convertase 1/3 (*PCSK1/3*) (10), melanocortin-4-receptor (*MC4R*) (11), and even a locus within the imprinted region of chromosome 15q, necdin (NDN) (12). Reduced expression of *NHLH2* in PWS patients could explain both the obesity and hypogonadal phenotypes of these patients. However, a significant gap in knowledge exists about how deletion of the paternal 15q region would lead to lower *NHLH2* levels.

Our expertise in *NHLH2* regulation and function, combined with the findings by Burnett and colleagues led us to ask if *SNORD116* might regulate *NHLH2* levels at a molecular level. We specifically focused on *SNORD116* due to the finding that the *Snord116*$^{m+/p-}$ mouse as well as iPSC derived neurons from patients with a minimal deletion that included *SNORD116* showed the lower *NHLH2/Nhlh2* protein and mRNA expression levels (3). In this paper, using *in silico* tools and a mouse hypothalamic neuron cell line, we demonstrate the mechanism by which *Snord116* controls levels of *Nhlh2*. Together, these results effectively change *SNORD116* from an orphan snoRNA, to one with a verified target, identify a *SNORD116* interaction motif that can be used to search for more targets, and provide a molecular genetic mechanism for how deletion of the 15q11-q13 region in humans leads to PWS.

Results

In silico determination of an *NHLH2: SNORD116–3* interaction motif

As the SNORD116 locus codes for orphan snoRNAs, meaning that there were no known interaction targets for any of its 30 snoRNAs, *in silico* tools were used to determine if any region of the *NHLH2* mRNA showed strong interactions with any of the 30 *SNORD116* snRNAs. Both the mouse and human *NHLH2* genes contain three exons, with only a small coding region at the beginning of exon 3, and a long 3′ untranslated region (UTR) (Fig. 1A). Within the 3'-UTR, several regions of high homology exist between mouse and human *NHLH2*. An *in silico* RNA:RNA interaction analysis using all of the Human *SNORD116* snoRNAs, and the human *NHLH2* mRNA sequence indicated that at least one of the 30 *SNORD116* transcripts had the potential to form a highly stable RNA:RNA interaction. As shown in Fig. 1A, the location of the putative interaction region is within a larger region showing 100% conservation between mouse and human *NHLH2* (as indicated by the gray shading). *In silico* RNA:RNA analysis identified other *SNORD116*:NHLH2 dyads with lower interaction energies (shown as arrow heads, Fig. 1A), but these interactions were not pursued further, as they did not interact with homologous regions in the mouse and human *NHLH2* mRNA, were not located in the snoRNA antisense region, and had much lower interaction energies compared to that for *SNORD116–3: NHLH2*. The putative *SNORD116–3: NHLH2* interaction motif is highly conserved in vertebrates (Fig. 1B-C). For *NHLH2,* this region is 100% conserved in the vertebrates shown (Fig. 1B), and in 70/77 vertebrates tested phylogenetically (data not shown). *SNORD116* consensus sequences for all paralogs within a cluster show high phylogenetic conservation in the predicted interaction region (Fig. 1C). Critically, the *SNORD116–3* predicted interaction is in the canonical antisense region just 5′ of the D′ box, conserved in all species shown (Fig. 1C). Of note, the *SNORD116–3* interaction motif on the *NHLH2* 3'UTR is found in 2 of 2 of the human *NHLH2* splice variants, and 2 of 2 of the murine splice variants that are registered in the RefSeq database (Supplementary Material, Fig. S1).

Numerous single nucleotide variants (SNV) exist within the NHLH2 and SNORD116–3 genomic loci, although none have been characterized as having clinical significance. However, an analysis of the effect of each naturally-occurring SNVs on the *NHLH2* 3'UTR in the region of this motif revealed five of these that disrupted the energy of interaction, as predicted using *in silico* RNA:RNA interaction analyses. Each of these disrupting SNVs were found towards the 3′ end of the motif (Fig. 2A) and reduce the predicted strength of interaction from −13.4 kcal/mol for the wildtype, to −9.4 for both rs1218168750 and rs1051613841 (Fig. 2B). As shown in Fig. 2C, compared to Fig. 2D rs1051613841 was predicted to disrupt the stem area of the *NHLH2:SNORD116–3* dyad. The predicted mouse secondary structure for the wildtype (Fig. 2E) and mutagenized form (Fig. 2F) are also shown.

The intact *NHLH2:SNORD116–3* interaction motif mediates high *Nhlh2* expression levels

N29/2 hypothalamic cells have been previously used to measure *Nhlh2* expression at the transcriptional and posttranscriptional levels (13,14). A set of constructs, using a myc-tag motif to differentiate endogenous *Nhlh2* from the transfected *Nhlh2* with different 3′ tails were used to measure Nhlh2 response to Snord116 in hypothalamic cells. These constructs all contained the myc-tagged *Nhlh2* (mouse) coding region linked to either high-expression SV40 3'UTR, a partial *Nhlh2* 3' UTR (13), a full-length *Nhlh2* 3'-UTR, or a full-length *Nhlh2* 3'-UTR containing the rs1051613841 SNV (Fig. 3A). Each were transfected into N29/2 hypothalamic neurons (15) which express low levels of *Snord116,* and *Nhlh2* during regular growth phase. Addition of a mouse *Snord116* consensus expression plasmid (which is most phylogenetically homologous to group 1 SNORD116 snoRNAs (16)) to cells expressing the full-length *Nhlh2-myc* mRNA construct led to a ∼15-fold increase of *Nhlh2-myc mRNA* levels (Fig. 3B). The construct containing the engineered SNV in the consensus motif, led to a smaller, yet still significant increase of ∼6-fold

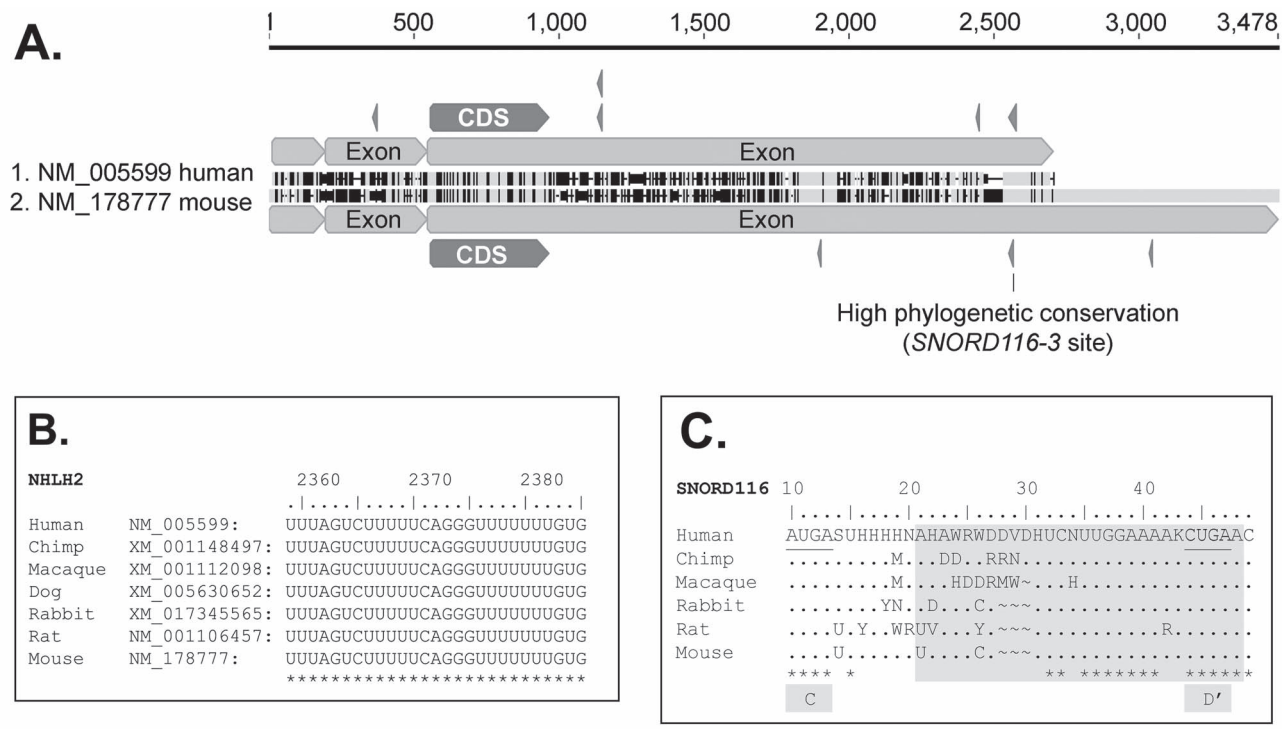

Figure 1. Strongest predicted RNA:RNA interaction between SNORD116 and NHLH2 is found within highly conserved regions. (**A**) Nucleotide alignment for human and mouse *NHLH2* mRNA sequences with predicted *SNORD116* interaction sites. Predicted interaction sites are displayed in small antisense arrows above or below the given sequence. Light gray regions in the aligned sequences show identity agreement, black regions show disagreements, and horizontal lines show gaps in alignment. One region with high phylogenetic agreement and predicted *SNORD116* interaction sites found in both human and mouse are labelled. (**B**) Phylogenetic alignment of *NHLH2* 3'UTR predicted interaction site among vertebrates. Nucleotide numbers above the alignment are based on human *NHLH2*, NM_005599. NCBI reference sequence numbers used for the analysis are shown. *indicates perfect non-ambiguous homology with the human sequence for all nucleotides in the site above. (**C**) Phylogenetic Alignment of consensus *SNORD116*. Underlines indicate C/D′ box motifs. Boxed region indicates predicted interaction site with *NHLH2*, which includes the canonical snoRNA antisense region. *indicates perfect non-ambiguous homology with the human sequence for all nucleotides in the site above. Human n = 30, chimp n = 28, rhesus n = 29, rabbit n = 29, rat n = 26, and mouse n = 17.

in *Nhlh2-myc* mRNA levels, while the partial tail without the predicted interaction site showed no increase in response to *Snord116* overexpression. Interestingly, the construct with the SV40 3'UTR showed a similar increase of ~5-fold, although the strongest predicted *Snord116* interaction site for this tail was a relatively weak (−5.54 kcal/mol) in the 3'UTR. Figure 3C shows that the different 3'UTR constructs lead to different steady-state *Nhlh2* protein levels, consistent with the mRNA levels. Like the protein levels, SV40 3'UTR shows greater baseline RNA expression when normalized across 3'UTR (Supplementary Material, Fig. S2). Snord116 overexpression ranged from about 100–1000-fold higher (Supplementary Material, Fig. S3). Of note, all constructs were under the control of the CMV promoter and had the identical *Nhlh2-myc* coding region through the *Nhlh2* stop codon. Thus, differences in expression level could only be attributed to differences in the 3'-UTR of the constructs, and the presence/absence of the putative motif. These data suggest that *Snord116* controls expression of *Nhlh2*, post-transcriptionally, through the 3'UTR motif identified by *in silico* binding analysis.

Snord116 snoRNA stabilizes *Nhlh2* mRNA

While post-transcriptional regulation of mRNA can be due to changes in mRNA translation efficiency, the 3'-UTR of an mRNA often directs regulation due to changes in mRNA stability. To test whether *Snord116* levels altered mRNA stability of *Nhlh2*, the same constructs as above and the N29/2 cell line was used in an actinomycin D assay. Actinomycin D (also known as dactinomycin) is an antibiotic and chemotherapeutic that inhibits DNA-dependent RNA synthesis through DNA intercalation and inhibition of RNA polymerase I, II, and III (17,18). As transcription of new mRNA is blocked when actinomycin D is added to a cell culture, the level of mRNA at times following addition of the chemical can be used to determine mRNA stability. As shown in Fig. 4, *Snord116* shows general overall stabilization of the SV40, Full, and SNV tails, throughout the 3-hour time course. This is consistent with *Snord116*'s effect on steady-state levels (Fig. 3B). The stabilization effect size is greater for the Full and SNV tails than SV40 (Fig. 4E). Additionally, this difference in stabilization effect size seems to be mediated by an early rapid decay of the Full/SNV tails without *Snord116*. About 50% of the RNA from the SNV/Full tails are degraded by 45 minutes, while both the partial/SV40 tails' levels remain higher ($p < 0.05$) and degrade to about 50% between 90–180 minutes (Fig. 4A-D). This indicates a relative baseline instability for the Full/SNV tails. This high initial decay rate within the first 45 minutes also slows down by the 90 min and 180 min intervals for Full/SNV tails (Supplementary Material, Fig. S4). Interestingly, with the addition of *Snord116*, this initially high rate of decay is blunted, indicating that *Snord116* has a protective effect against RNA decay within the first 45 minutes for the Full/SNV tails (Fig. 4G). Critically, the *Snord116* protective effect at 45 minutes trends to being less effective for the SNV tail when compared to the full tail but does not reach a significance difference between the two ($p = 0.10$). Of

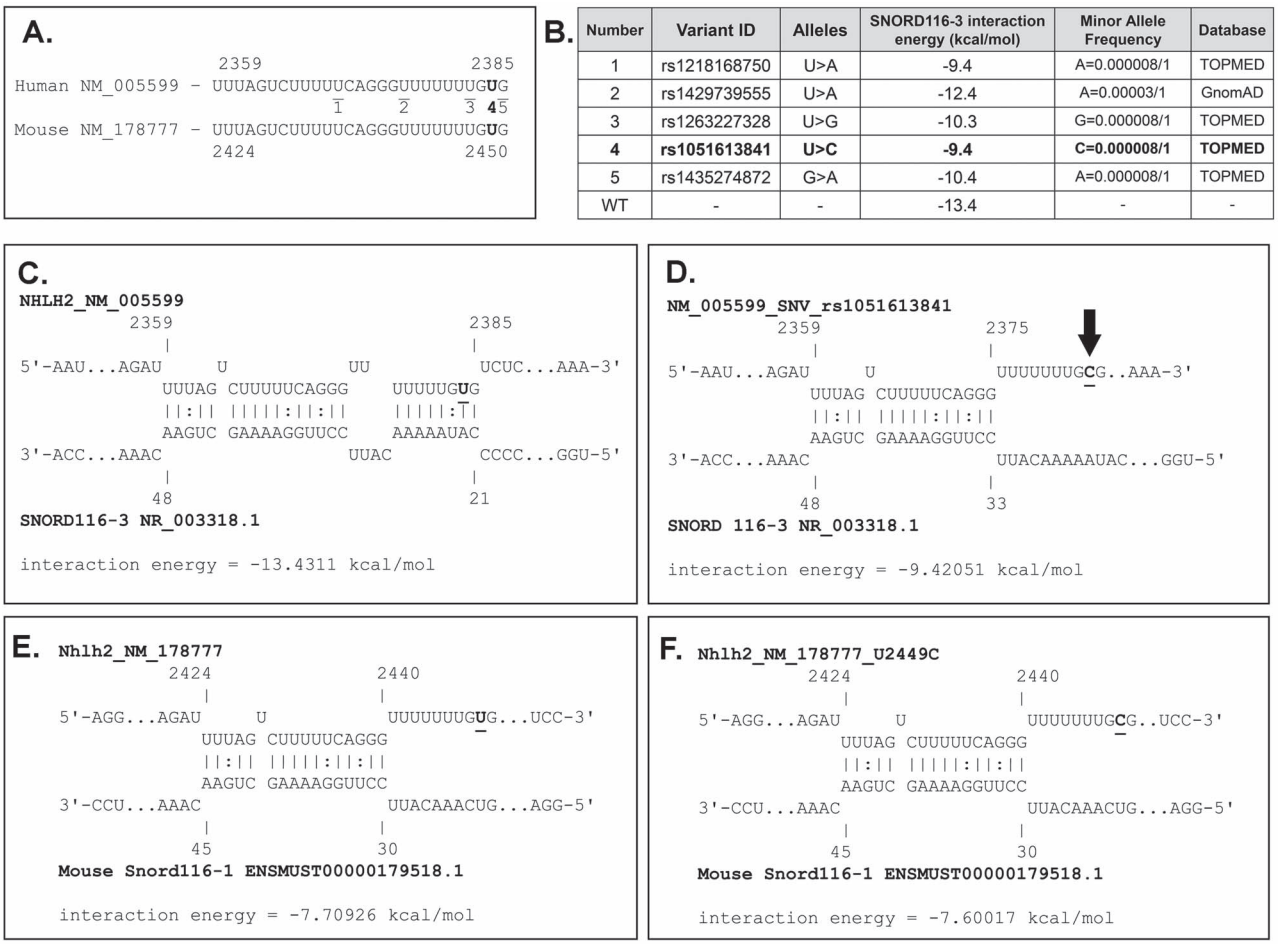

Number	Variant ID	Alleles	SNORD116-3 interaction energy (kcal/mol)	Minor Allele Frequency	Database
1	rs1218168750	U>A	-9.4	A=0.000008/1	TOPMED
2	rs1429739555	U>A	-12.4	A=0.00003/1	GnomAD
3	rs1263227328	U>G	-10.3	G=0.000008/1	TOPMED
4	**rs1051613841**	**U>C**	**-9.4**	**C=0.000008/1**	**TOPMED**
5	rs1435274872	G>A	-10.4	A=0.000008/1	TOPMED
WT	-	-	-13.4	-	-

Figure 2. Single nucleotide variants have the potential to reduce the predicted *NHLH2: SNORD116* motif interaction energy. (**A**) RNA alignment of the predicted *SNORD116* interaction region for mouse and human *NHLH2* with five human SNVs displayed. (**B**) Reference SNV data provided from NCBI SNP database, including accession number, and minor allele frequency (MAF). The predicted effect on the *SNORD116–3* interaction energy (kcal/mol) with *NHLH2* is shown. (**C**) INTA-RNA predicted structure of the wild-type *NHLH2:SNORD116–3* interaction. (**D**) INTA-RNA predicted structure of the *NHLH2:SNORD116–3* interaction containing *NHLH2* SNV rs1051613841 (**E**) INTA-RNA predicted structure of the wild-type mouse *Nhlh2:Snord116* interaction used in the current study. (**F**) INTA-RNA predicted structure of the mutagenized mouse sequence U2449C. SNV site of interest is labelled in bold, underlined, and/or with arrows.

note, Snord116 RNA does not decay over time (Supplementary Material, Fig. S5).

Discussion

Snord116 has been previously implicated in changes of gene expression, with proposed molecular mechanisms including alternative splicing and RNA-stability (3,19–21). The current study is the first to demonstrate that RNA stability indeed is a molecular mechanism for *Snord116*-dependent changes in gene expression. As this study was done using cell lines and molecular constructs, there are minimal confounds from the PWS locus and the *Snord116* host gene (*116HG*). Rather, these results can be directly attributed to a *Snord116* snoRNA and its target gene.

The current study is the first to show evidence for an interaction of *Snord116* RNA with a predicted target. Although RNA interaction prediction for targets of *SNORD116* have been performed previously, there was no experimental validation of these interactions (19,22). Using the snoTARGET software (22), previous predictions failed to include *NHLH2* as a potential target. Furthermore, the predicted strength of interaction with *NHLH2* is relatively low compared to other predicted target RNAs. The current study suggests that while interaction prediction is a useful tool, as implicated by the predicted effect of the SNV on the 3'UTR:Snord116 interaction, other factors, such as protein or other interactions should be considered.

Using both the data in this paper, and previous work, we predict that high *NHLH2* levels may be present in cells expressing *SNORD116* and/or treated with leptin. *Snord116* expression from wild type mouse hypothalamus may increase with refeeding after overnight fasting (3). As both leptin and *Snord116* levels increase during a refeeding period, these two paths appear to converge synergistically on *Nhlh2* upregulation: transcriptional upregulation of *Nhlh2* through leptin signaling (14), and post-transcriptional upregulation of *Nhlh2* through *Snord116*. While some previous studies have not detected changes in the levels of hypothalamic *NHLH2* mRNA in PWS patient post-mortem tissue or PWS model mice (19–21), our data suggest that changes in *Nhlh2* levels may occur with a short temporal window that the other studies failed to capture. Conversely, another study has demonstrated that growing lymphoblastoid cells derived from PWS patients show a – 1.5 fold expression of NHLH2 mRNA compared to normal lymphoblastoid cells (23).

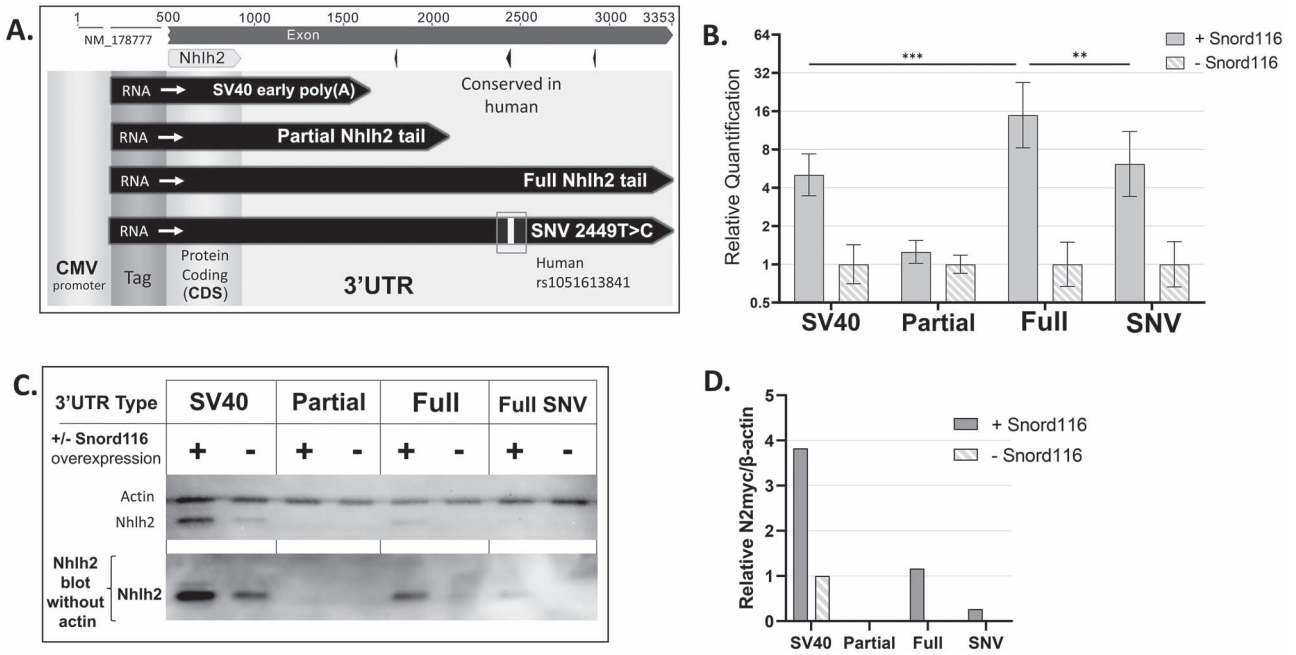

Figure 3. Post-transcriptional Regulation of *Nhlh2* by *Snord116* is reduced by a SNV in the predicted interaction region within the *Nhlh2* 3'UTR. (**A**) Reporter plasmids expressing mouse *Nhlh2* mRNA. Mouse *Nhlh2* mRNA (NM_178777) with annotated exons, coding sequence (CDS), and predicted *Snord116* interaction sites. Four different expression vectors for tagged *Nhlh2* mRNA with varying 3'UTRs are shown to scale in comparison to *Nhlh2* mRNA. The mouse vector was engineered to contain a T > C SNV within the predicted interaction region which is shown by the white bar on that vector. (**B**) Relative expression of tagged *Nhlh2* RNA with different 3'UTRs during *Snord116* overexpression in N29/2 cells. *Nhlh2* SNV at predicted *Snord116* interaction site decreases *Snord116*-induced fold change. For the +Snord116 condition, one-way ANOVA $F(3,29) = 30.992$, $p < 0.001$ with Bonferroni correction shows the only 3'UTR types to not be significantly different to each other are SV40 and SNV. All other comparisons are significantly different ($p < 0.05$); $N = 6$ for partial 3'UTR conditions; $N = 9$ for SV40, Full, and SNV conditions. Error bars indicate ±SD. $^{**}p < 0.01$, $^{***}p < 0.001$. Statistical analysis performed on respective ddCT values from which Relative Quantification (RQ) values are derived. (**C**) Representative Western blot shows higher protein translation of the +Snord116 conditions and the SV40 3'UTR construct. Both blots are from the same samples but the bottom blot is with anti-myc tag antibody alone to allow for longer signal development. Note the western blot is normalized across 3'UTR type, unlike Figure 3B. (**D**) Optical density of representative Western blot.

It may be questioned if the current study is relevant to the biological levels of the genes in question. In our approximation, when compared to mouse hypothalamus tissue by RT-QPCR, the current study's *Snord116* levels are greatly under-expressed, and *Nhlh2* levels range from equal expression to slight under-expression (data not shown). Part of the rationale for using the N29/2 cell line is that *Snord116* levels are low, replicating a PWS-like condition, and allowing specific overexpression of exogenous *Snord116*. Precise quantification of these data between a cell line and whole mouse hypothalamus presents issues, due to a lack of suitable validated reference genes for RT-QPCR appropriate for use. Considering raw CT values and equal total RNA per RT-QPCR reaction, endogenous *Snord116* in mouse hypothalamus is 8000—100 000-fold higher than our overexpression conditions in N29/2 cells. This general pattern of expression is a large enough difference that the authors are comfortable coming to this general estimate and conclusion for *Snord116* levels between cell-line and tissue. However, it must be addressed that RT-QPCR of *Snord116* can sense both the non-spliced *Snord116* host gene, and the mature *Snord116*, so this too may partially explain the large difference between N29/2 cells and mouse hypothalamus levels.

The current study shows that high expression of *Snord116* leads to higher stability of *Nhlh2* mRNA and subsequently, higher levels of translated protein. At steady-state levels, the SNV 3'UTR seems to disrupt *Snord116*-dependent upregulation when compared to the full wildtype 3'UTR, implying that the predicted interaction site is playing a role in *Snord116* interaction (Fig. 3B). However, this disruption from the SNV is not seen in the RNA decay experiment (Fig. 4). The *Snord116* protective effect at 45 minutes only trends to being less effective for the SNV tail when compared to the full tail ($p = 0.10$). This may be due to some differences between steady-state and RNA decay experiments. The steady-state experiment may be sensitive to the accrual of RNA over a 24-hour period post-transfection and any RNA stability differences may lead to a cumulative effect. The RNA decay experiment is sensitive to a smaller timeframe, and highlights that the initial 45 minutes may be critical for stabilization effects between the Full and SNV 3'UTRs. Therefore, small differences in stability that do not show statistical significance at 45 minutes may be amplified when these small differences accumulate over time and show differences at steady-state levels. Additionally, it is possible that a more disruptive SNV may show stronger effects than the one used in the current study. Furthermore, the steady-state experiment did not include a media refresh prior to cell lysis, while the RNA decay experiment refreshed the media with the addition of Actinomycin D at the 0-minute timepoint, which could add a serum or media factor that affects expression levels.

While the current study implies *Snord116* stabilizes target RNAs, it is possible that results from steady state experiments are influenced by differences in transcription (Fig. 3B). However, the consistent pattern of effect size between steady-state and RNA decay studies implies that RNA stability is playing a major role. Future work will have to examine possible effects on transcription.

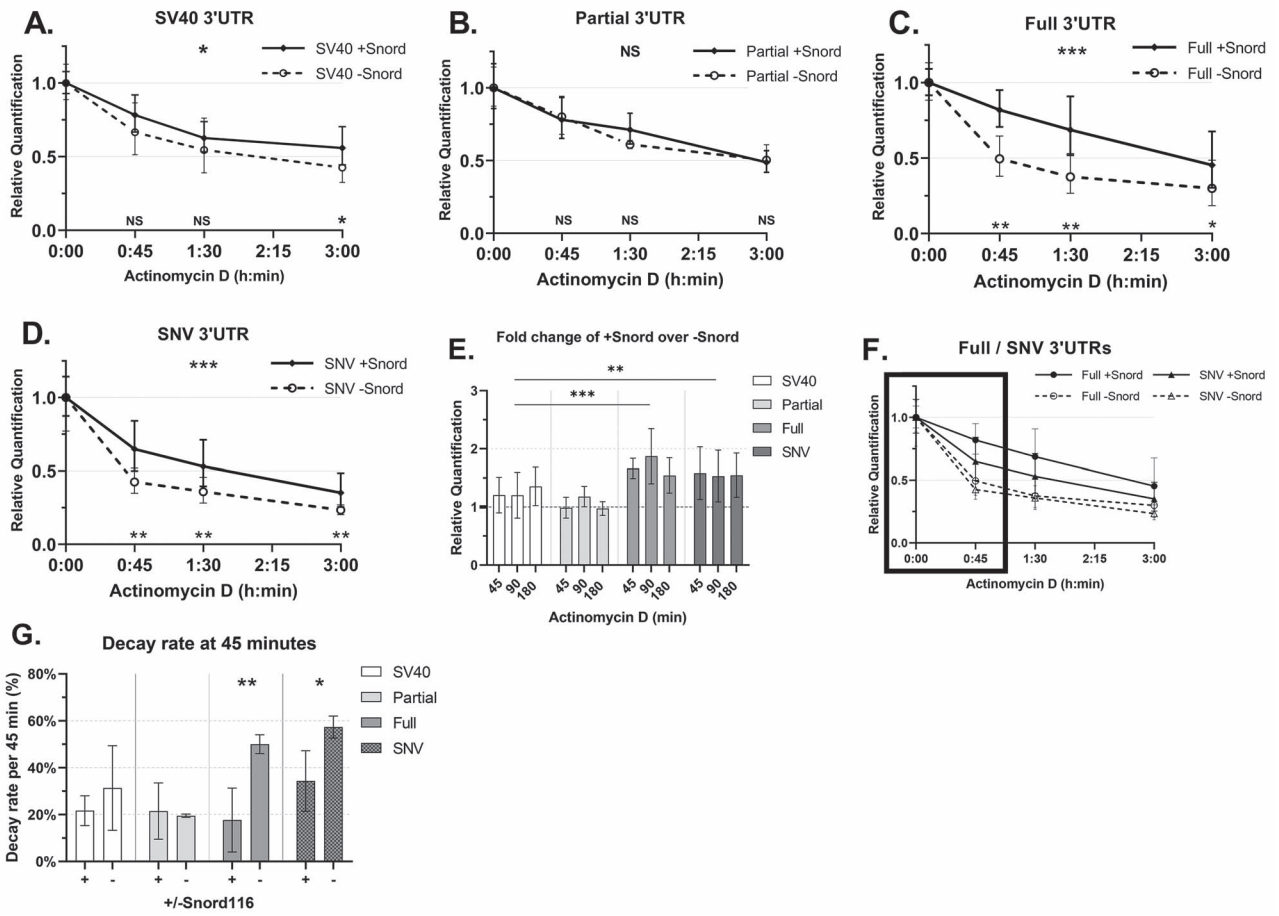

Figure 4. *Snord116* stabilizes target RNAs and protects against early rapid decay dependent on 3'UTR. (**A-D**) Relative expression of reporter mRNAs with different 3'UTRs during *Snord116* overexpression and actinomycin D treatment. *Snord116* overexpression indicated by solid lines, and negative control indicated by dotted lines. Significance indicators for main effect across all time points between +/-Snord116 are shown just below the title of each figure. Significance indicators for individual time points between +/-Snord116 are shown just above the X-axis. (**E**) Fold change of +Snord116 relative to -Snord116 condition for each 3'UTR and time point. (**F**) Relative expression of Full and SNV 3'UTRs modified from Fig. 4C-D. Boxed area emphasizing 45-minute time point for the context of Fig. 4G. (**G**) Decay rate shown as percent decay for the 45-minute time point for each 3'UTR and Snord116 condition. Significance indicators correspond to differences between +/-Snord116 conditions within a 3'UTR condition. N = 6 for partial 3'UTR condition; N = 9 for SV40, Full, and SNV conditions. Error bars indicate ±SD. $^{*}p < 0.05$, $^{**}p < 0.01$, $^{***}p < 0.001$, $^{NS}p > 0.05$.

The use of the *Snord116* expression construct minimizes confounds associated with the PWS genomic locus, as there are many species of ncRNAs and host genes expressed from the locus (24–26). Use of the N29/2 neuronal cell line, which has endogenously low levels of *Snord116* lends confidence that the results shown are due to an overexpression of *Snord116* rather than changes in the many host genes and ncRNAs found at the PWS genomic locus that are often associated with a genomic deletion. It is worth noting that the construct used contains *Snord116* within its natural intron, as this is necessary for proper snoRNA maturation and processing (20). The natural genomic processing of the *Snord116* host gene (*116HG*) results in a much longer ncRNA with many exons that are not within the construct used (24,27). There is no way to completely exclude a requirement for the endogenous host gene or other genes within the PWS locus which are present in N29/2 cells. Expression levels of *116HG* were not tested in the present study, while *Snord116* snoRNA levels were tested by RT-QPCR to validate overexpression (Supplementary Material, Figs S3 and S5).

Use of the SNV-containing construct appears to confirm that the interaction motif is within the predicted regions on both *Nhlh2* and *Snord116*. Based on this, a model was created that predicts the secondary structure and interaction between *NHLH2* and *SNORD116–3* (Fig. 5). As shown in the prediction, interaction with *SNORD116–3* occurs within a stem-loop structure on the *NHLH2* 3'UTR. In examining the structure, the stem-loop may be either stabilized or disrupted by *SNORD116–3* interactions, which likely depends on RNA-binding protein interactions within that region. Of interest, hnRNP-U has previously been shown to stabilize *NHLH2* mRNA, although the position of that interaction is not known (28). Thus, while the most well-established mechanism of non-methylating SNORDs is through pre-mRNA splicing (20), enhancement of mRNA stability by SNORDs remain a tantalizing mechanism. It remains to be seen whether the mRNA stability observed in the current study is through the canonical SNORD mechanism of 2'-O methylation or non-canonical mechanisms.

While the predicted RNA interaction in *Nhlh2* 3'UTR and the SNV results indicate a possible direct RNA:RNA interaction region, the increased mRNA stability seen with the SV40 3'UTR indicate that *Snord116*'s mRNA stability effect may be non-specific. The predicted interaction between *Snord116* and the SV40 3'UTR is relatively weak and does not correspond to the *Snord116* antisense target region (Supplementary Material, Fig. S6). This differs from the *Nhlh2* 3'UTR that is predicted to be complementary to the *Snord116* antisense target region. These results suggest that *Snord116* may have general effects on RNA

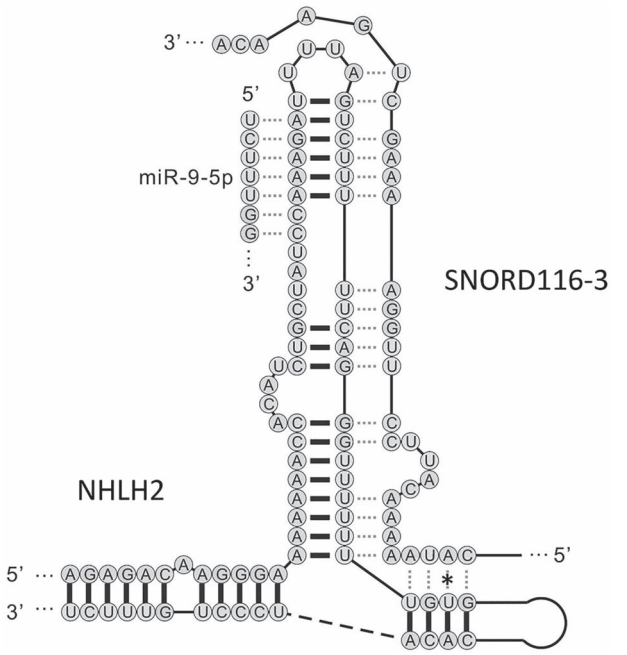

Figure 5. Predicted model of *SNORD116:NHLH2* interaction. The ViennaRNA package software was used to predict the folding structure for *NHLH2* 3'UTR, and then the interaction with *SNORD116*. The miR-9-5p interaction site was identified using TargetScan. Both interactions were added to the overall structure for viewing of their relative positions on the *NHLH2* 3'UTR only, not to indicate whether one or both simultaneously interaction with the stem-loop structure. *indicates the site of the *NHLH2* SNV used in the current study.

stability independent of sequence complementarity. However, the partial 3'UTR is unaffected by *Snord116* indicating that *Snord116*'s effect may be dependent on RNA sequence and potential co-factors.

In examining the *NHLH2* RNA sequence around the putative *SNORD116* interaction motif using RegRNA 2.0 (29), there are no overlaps of known motifs within the putative *SNORD116* interaction motif. However, a poly(A) signal is about 100 bp downstream of the predicted interaction site for both mouse and human. The mouse transcript has a splice variant that ends at this poly(A) signal (XM_006501112), while the one used in the current study is the splice variant with the longest 3'UTR (NM_178777) (Supplementary Material, Fig. S1). *Snord116* may be mediating it's RNA stability effect through poly(A) signal pathways, as the partial 3'UTR RNA used in the current study does not contain a strong poly(A) signal, while the SV40 3'UTR does. Additionally, in mouse *Nhlh2,* but not human, there is a 60-72 nt (depending on strain) trinucleotide repeat region of GAA about 20 nt upstream of the predicted *Snord116* interaction region. This region is predicted to be an exon splicing enhancer, although there is little evidence of any splice variants using this exon splice site. Furthermore, just five base pairs upstream from the interaction site is a putative microRNA interaction site, predicted using TargetScanHuman (30). Both the *SNORD116* and miR-9-5p sites lie within the predicted stem-loop structure on the *NHLH2* mRNA 3'UTR (Fig. 5). *MiR-9-5p* is a neuronally-expressed microRNA whose dysregulation has been implicated in a number of neurodegenerative diseases (31). Interestingly, interaction with *miR-9-5p* has been shown to decrease target mRNA stability (32,33). Experiments to examine if *SNORD116* disrupts the *NHLH2* stem-loop structure are out of the scope of this study, but would allow one to determine if *miR-9-5p* directly binds to and increases the stability of *NHLH2* mRNA. In either scenario, the possible interaction with *miR-9-5p* or other secondary factors, including proteins may explain why the SNV had a weaker effect overall on *Nhlh2* stability levels than we had predicted using *in silico* tools, and suggest that a second region mediating additional mRNA stability control for *NHLH2* may occur outside of the predicted *NHLH2:SNORD116* interaction motif. The entire region shown in Fig. 5 has high homology in vertebrates (data not shown). Phylogenetic conservation of small motifs in untranslated regions suggest a functional conservation (34,35) that can be used to predict and test functional interactions, as was done herein. This longer region within the *NHLH2* 3'UTR can be used to identify other possible *SNORD116*–3 targets that may also contain this motif in their 3'-UTR. Likewise, as all of the *SNORD116* snoRNAs within group 1 are highly conserved but still have some nucleotide-based substitutions between them (16), we can use this information to determine if all group 1 snoRNAs can interact with similar targets or whether each has a specific set of targets with highly conserved/high energy interaction. Indeed, as shown by our work, a single SNV on the target mRNA can reduce the ability of overexpressed *Snord116* RNA to stabilize the target mRNA. It is possible that the reverse is true as well—with SNVs within the *SNORD116* locus possibly leading to PWS-like phenotypes.

While we do not find an exact match to the *NHLH2:SNORD116* motif in the *PCSK1* mRNA or other RNA-seq identified RNAs to date (3), it is possible that a similar motif, and different *SNORD116* cluster snoRNAs contribute to these downregulations in PWS models. It is also possible that downregulation of *PCSK1* and other mRNAs in neuronally-induced PWS stem cells simply results from the loss of direct, leptin-induced transcriptional regulation by *NHLH2, as* we have previously shown for *Pcsk1* (10). Additionally, there is a convincing mechanism for *PCSK1* downregulation through *MAGEL2* loss in PWS patients with a large deletion of the genomic locus (36). However, these findings do not explain the low levels of *PCSK1* mRNA and protein found in a PWS microdeletion model of neuronally differentiated iPSCs containing a genomic deletion of only *SNORD109A, SNORD116* cluster, and *IPW* (3). Additionally, PWS mouse models with intact *Magel2* and loss of the paternal *Snord116* cluster have lower levels of *Pcsk1* mRNA and protein in islet cells and stomach (3,36). These data suggest that loss of *Snord116* may lead to downregulation of *Nhlh2*-dependent *Pcsk1* in addition to the *MAGEL2* mechanism. This may add to the ongoing explanation of why PWS patients with large genomic deletions show stronger phenotypes.

NHLH2 is a basic-helix–loop–helix transcription factor, with multiple known and putative targets (9–11,37–39). Many of these targets (i.e. *PCSK1, MC4R*) are involved in neuronal control of body weight, and may provide an explanation for some of the phenotypes of PWS. *SNORD116*-mediated post-transcriptional regulation of *NHLH2* could result in hundreds of downstream regulatory changes. For PWS patients, these data now suggest why PWS patients, and the *Nhlh2* knockout mouse share many of the same phenotypes (3,9), and may open further analyses into therapeutic interventions that can increase levels of *NHLH2* or one of its transcriptional targets, even in individuals with impaired *SNORD116*.

Materials and Methods

Nucleotide Alignments

Nucleotide alignment and annotation performed using Geneious Prime 2020.1.2 (https://www.geneious.com, Biomatters, New

Zealand). The 'Geneious alignment' algorithm on default settings was used for pairwise nucleotide alignment of human and mouse sequences with annotations. Phylogenetic nucleotide alignment of *SNORD116* was based on original alignments from Kocher and Good (16).

RNA–RNA Interaction Prediction

IntaRNA version 2.4.0 (40–43) was used with default parameters to predict the interaction structures between SNORD116 and its targets. Specifically, the entire mRNA sequence of NHLH2 (Gene ID: 4808) was input for analysis. IntaRNA is an algorithm that computes an interaction structure with minimum free energy from two input sequences using dynamic programming routine. All secondary structures of single stranded RNA are predicted by ViennaRNA 2.0 (44).

Generation of Constructs

The *Nhlh2*-myc tagged construct with SV40 p(A) tail was a generous gift from Dr Thomas Braun, Max Planck Institute, Bad Nauheim, Germany. This construct contained in the pCS2-MT backbone was used to generate the *Nhlh2*-myc tag with a partial 3'UTR used in a previous study (13). The partial 3'UTR construct was then used for generating the full 3'UTR and the full 3'UTR containing the rs1051613841 SNV. Specifically, a separate vector containing the 1145 bp of extra 3'UTR cDNA was cloned using PCR amplification with PstI sites on the 5′ and 3′ ends of the PCR product, and subsequently cloned into a PstI site at the end of the partial 3'UTR. This vector containing the full 3'UTR was then used to create the SNV construct by site-directed mutagenesis using the Phusion Site-Directed Mutagenesis Kit (ThermoFisher # F541), and mutagenesis primers (Supplementary Material, Table S1). The myc-tags on these constructs allow for QPCR analysis of tagged RNA separate from endogenous RNA and allow for primary antibody detection for Western blotting.

The mouse *Snord116* expression vector was a generous gift from Dr Stefan Stamm, University of Kentucky, Lexington, USA (20). This construct was used to generate a negative control vector for *Snord116* expression by excising the *Snord116* insert using MssI digestion (2722 bp), and ligation of the blunt ended fragment of interest (5035 bp). This left a backbone nearly identical to the pCDNA5/FRT/TO vector, but missing 102 bp of the multiple cloning site in between the CMV promoter and bGH p(A) terminator.

All constructs were sequenced and subjected to restriction enzyme digests followed by agarose gel electrophoresis for validation of cloning procedures.

Cell Culture and Transfections

The mouse hypothalamus neuron cell line, N29/2 (15), was maintained in T25 flasks in DMEM (4.5 g/L glucose, with 110 mg/L sodium pyruvate) (ThermoFisher # 11995065) and 10% fetal bovine serum (GE Healthcare #SH30396.03HI) with penicillin (50 units/mL)/streptomycin (50ug/mL) (Thermo # 15070063) at 4–6% CO2 and 37°C. Cells were detached from flasks using trypsin–EDTA (ThermoFisher # 25300054) and 6-well plates were seeded with 2 x 10^4—10^5 cells per well. Transfections were done 2–4 days post seeding using Opti-MEM® media (ThermoFisher # 31985070) and Lipofectamine® 3000 (ThermoFisher #L3000008) according to manufacturer's instructions at 60–90% cell confluence. All transfections were performed between 3 p.m. and 6 p.m. 200 ng of each plasmid DNA was transfected for Leptin receptor, *Stat3*, +/-*Snord116*, *Nhlh2*-myctag for a total of 800 ng DNA per well of a 6-well plate. Leptin receptor and *Stat3* expression vectors were included to ensure the expression of these key regulatory components of *Nhlh2* and for consistency with previous studies of *Nhlh2* (10,11,13,14).

RNA Purification

24 hours post transfection, cell culture media was removed, and cells were lysed with 1 mL of TRIzol® Reagent (ThermoFisher #15596018) directly in 6-well culture plates. TRIzol samples were frozen at −20°C in microfuge tubes until purified (1–14 days) using the TRIzol+Purelink RNA minikit (ThermoFisher #12183025) following manufacturer's instructions for the TRIzol® Plus Total Transcriptome Isolation protocol. Purified RNA was then DNAse treated using TURBO DNA-free™ Kit (ThermoFisher #AM1907) according to manufacturer's instructions, diluted to 60 ng/μL in nuclease-free water, and stored at −80°C.

Reverse-Transcriptase Quantitative PCR

For RT-QPCR, Power SYBR® Green RNA-to-CT™ 1-Step Kit (ThermoFisher #4389986) was used according to manufacturer's instructions. 10uL reactions were performed using 150 nM final primer concentration. Primers were assessed for efficiency using a dilution series and fell within 90%–110% efficiency. 90 ng RNA was used per 10uL reaction. Two technical replicates were performed. Control reactions for each sample (No reverse-transcriptase and no-template controls) were used for quality control. 384-well plates were run on the ViiA 7 Real-Time PCR System (ThermoFisher) according to RT-QPCR mix instructions and thermocycling conditions were not modified from suggested protocol (1-step annealing/extension at 60°C). Quality control measures including melt-curve analysis, technical replicate analysis, etc. were analyzed by thermocycler software and by operator; any major errors were excluded from analysis when appropriate, and/or new samples and plates were run when appropriate. Candidate reference genes for ddCT analysis were analyzed for appropriate reference controls. Mouse beta-actin was used as reference gene control for steady-state experiments. Potential reference genes were evaluated for the Actinomycin D experiments, but none were satisfactory and thus no reference gene was used for RNA decay experiments. The CT values used reflect molarity of the target RNA, as total RNA remained the same for each reaction (90 ng). Relative change in molarity over the RNA decay time course is thereby relative to the average decay of total RNA (e.g. If a target gene's relative quantification stays at 1.0 throughout the 180 minutes of Actinomycin D treatment, it decays at the same rate as the total RNA average decay rate).

Western Blot

Constructs were transfected into N29/2 cells, and 24 hours following transfection, cells were washed, lysed in RIPA buffer, scraped from the tissue culture plates, and processed for Western analysis using standard methods. Equal amounts of protein (7 μg/lane), as determined using Bradford Reagent (AMRESCO #E530-1 L) were separated on a 12% SDS polyacrylamide gel and transferred to PVDF membrane. Western blotting was performed using rabbit anti-myctag polyclonal primary antibody (Proteintech #16286–1-AP) with goat anti-rabbit horseradish peroxidase-linked antibody as a secondary antibody. Chemiluminescent signal was detected using the SuperSignal™ West Femto Maximum Sensitivity Substrate (ThermoFisher #34095).

RNA stability assay

24 hours post-transfection, cell culture media was refreshed with 5 µg/ml Actinomycin D (Sigma #SBR00013-1ML) for 45, 90, and 180 minutes before lysis with Trizol directly in 6-well plates. The 0-minute timepoints were refreshed with media containing no Actinomycin D for 50 minutes before lysis. Plates with Actinomycin D were concealed from light during the duration of Actinomycin D incubation. The full time-course experiment was replicated 3 independent times with 3 separate vials of frozen N29/2 cells.

Statistical Analysis

All RT-QPCR data were analyzed using Microsoft Excel 16 for Microsoft 365, IBM SPSS Statistics 26 for Windows, and GraphPad Prism 9.0.0. N = 6 for partial 3'UTR conditions; N = 9 for SV40, Full, and Full SNV conditions. Error bars indicate ±SD. The 2^{ddCT} method of relative quantification was used. Statistical significance tests performed on respective ddCT values from which Relative Quantification values are derived. Significance is expressed at $^{*}p < 0.05$, $^{**}p < 0.01$, $^{***}p < 0.001$, $^{NS}p > 0.05$.

For steady-state experiments, a two-way ANOVA with Bonferroni correction was used for relative expression of tagged RNA normalized within 3'UTR type. CT and dCT values used are provided in Supplementary Material, File S1.

For RNA decay analysis, CT values were normalized to the average CT of the 0-minute time point within a transfection, within 3'UTR condition, and within Snord116 condition [CT(0.minute.average)-CT(individual.value)]. 0-minute-normalized CT values (0dCT) were then pooled across transfection trial and assessed for normality. For Fig. 4A-D, 2-Way ANOVAs with Šídák's multiple comparisons test within timepoints were run on each 3'UTR excluding the 0-min timepoints. 2^{0dCT} are displayed in Fig. 4A-D. For Fig. 4E, +Snord116 CTs were normalized to average -Snord116 CTs within transfection trial, 3'UTR, and timepoints. [CT(-Snord116.average(TransfectionTrial'x'.Timepoint'y'.3'UTR'z'))-CT(individual.value(TransfectionTrial'x'.Timepoint'y'.3'UTR'z'))] These -Snord116 normalized CT values were analyzed using 2-Way ANOVA with Šídák's multiple comparisons test excluding 0-minute timepoints. $2^{(-snord116.normalized.CTs)}$ are graphed. For decay rate, 0-minute-normalized CT values were used to calculate CT differences between one timepoint and the next successive timepoint and adjusted for 45-minute intervals. Individual CT values were normalized to the average CT value of the previous timepoint within a condition. These values were used to perform 2-Way ANOVAs with Šídák's multiple comparisons test within 3'UTR, shown in Fig. 4G and within 3'UTR/Snord116 for Supplementary Material, Fig. S4. Normalized CT values were adjusted to percentage values for graphs [(1-($2^{(decay.rate.normalized.CT)}$))*100]. CT values used are provided in Supplementary Material, File S2.

Supplementary Material

Supplementary Material is available at *HMG* online.

Acknowledgements

We would like to thank Joe Grieco (Virginia Tech) for his assistance in Western Blots and Dr Stefan Stamm (University of Kentucky), for the gift of the mouse Snord116 expression vector. The work was funded by a grant (#532939) from the Foundation for Prader-Willi Research (FPWR) to D.J.G., an internal grant from the Adaptive Brain and Behavior Destination Area at Virginia Tech to D.J.G, and a student research award from Sigma Xi to M.A.K.

Conflict of Interest Statement. D.J.G. receives funding from the BASF Chemical Company, Berkeley, CA for a PWS-related project, but none of these funds were used for the project reported herein.

References

1. Butler, M.G., Miller, J.L. and Forster, J.L. (2019) Prader-Willi syndrome - clinical genetics, diagnosis and treatment approaches: an update. *Curr. Pediatr. Rev.*, **15**, 207–244.
2. Tan, Q., Potter, K.J., Burnett, L.C., Orsso, C.E., Inman, M., Ryman, D.C. and Haqq, A.M. (2020) Prader-Willi-like phenotype caused by an atypical 15q11.2 microdeletion. *Genes (Basel)*, **11**, 128. doi: 10.3390/genes11020128.
3. Burnett, L.C., LeDuc, C.A., Sulsona, C.R., Paull, D., Rausch, R., Eddiry, S., Carli, J.F., Morabito, M.V., Skowronski, A.A., Hubner, G. *et al.* (2017) Deficiency in prohormone convertase PC1 impairs prohormone processing in Prader-Willi syndrome. *J. Clin. Invest.*, **127**, 293–305.
4. Coyle, C.A., Jing, E., Hosmer, T., Powers, J.B., Wade, G. and Good, D.J. (2002) Reduced voluntary activity precedes adult-onset obesity in Nhlh2 knockout mice. *Physiol. Behav.*, **77**, 387–402.
5. Cogliati, T., Delgado-Romero, P., Norwitz, E.R., Guduric-Fuchs, J., Kaiser, U.B., Wray, S. and Kirsch, I.R. (2007) Pubertal impairment in Nhlh2 null mice is associated with hypothalamic and pituitary deficiencies. *Mol. Endocrinol.*, **21**, 3013–3027.
6. Good, D.J., Porter, F.D., Mahon, K.A., Parlow, A.F., Westphal, H. and Kirsch, I.R. (1997) Hypogonadism and obesity in mice with a targeted deletion of the Nhlh2 gene. *Nat. Genet.*, **15**, 397–401.
7. Morales, J.S., Valenzuela, P.L., Pareja-Galeano, H., Rincon-Castanedo, C., Rubin, D.A. and Lucia, A. (2019) Physical exercise and Prader-Willi syndrome: a systematic review. *Clin. Endocrinol.*, **90**, 649–661.
8. Bekx, M.T., Carrel, A.L., Shriver, T.C., Li, Z. and Allen, D.B. (2003) Decreased energy expenditure is caused by abnormal body composition in infants with Prader-Willi syndrome. *J. Pediatr.*, **143**, 372–376.
9. Good, D.J. and Braun, T. (2013) NHLH2: at the intersection of obesity and fertility. *Trends Endocrinol. Metab.*, **24**, 385–390.
10. Fox, D.L. and Good, D.J. (2008) Nescient helix-loop-helix 2 interacts with signal transducer and activator of transcription 3 to regulate transcription of prohormone convertase 1/3. *Mol. Endocrinol.*, **22**, 1438–1448.
11. Wankhade, U.D. and Good, D.J. (2011) Melanocortin 4 receptor is a transcriptional target of nescient helix-loop-helix-2. *Mol. Cell. Endocrinol.*, **341**, 39–47.
12. Kruger, M., Ruschke, K. and Braun, T. (2004) NSCL-1 and NSCL-2 synergistically determine the fate of GnRH-1 neurons and control necdin gene expression. *EMBO J.*, **23**, 4353–4364.
13. Al Rayyan, N., Wankhade, U.D., Bush, K. and Good, D.J. (2013) Two single nucleotide polymorphisms in the human nescient helix-loop-helix 2 (NHLH2) gene reduce mRNA stability and DNA binding. *Gene*, **512**, 134–142.

14. Al Rayyan, N., Zhang, J., Burnside, A.S. and Good, D.J. (2014) Leptin signaling regulates hypothalamic expression of nescient helix-loop-helix 2 (Nhlh2) through signal transducer and activator 3 (Stat3). *Mol. Cell. Endocrinol.*, **384**, 134–142.
15. Belsham, D.D., Cai, F., Cui, H., Smukler, S.R., Salapatek, A.M. and Shkreta, L. (2004) Generation of a phenotypic array of hypothalamic neuronal cell models to study complex neuroendocrine disorders. *Endocrinology*, **145**, 393–400.
16. Good, D.J. and Kocher, M.A. (2017) Phylogenetic analysis of the SNORD116 locus. *Genes (Basel)*, **8**, 358. doi: 10.3390/genes8120358.
17. Sobell, H.M. (1985) Actinomycin and DNA transcription. *Proc. Natl. Acad. Sci. U. S. A.*, **82**, 5328–5331.
18. Sobell, H.M., Jain, S.C., Sakore, T.D. and Nordman, C.E. (1971) Stereochemistry of actinomycin–DNA binding. *Nat. New Biol.*, **231**, 200–205.
19. Bochukova, E.G., Lawler, K., Croizier, S., Keogh, J.M., Patel, N., Strohbehn, G., Lo, K.K., Humphrey, J., Hokken-Koelega, A., Damen, L. *et al.* (2018) A transcriptomic signature of the hypothalamic response to fasting and BDNF deficiency in Prader-Willi syndrome. *Cell Rep.*, **22**, 3401–3408.
20. Falaleeva, M., Surface, J., Shen, M., de la Grange, P. and Stamm, S. (2015) SNORD116 and SNORD115 change expression of multiple genes and modify each other's activity. *Gene*, **572**, 266–273.
21. Polex-Wolf, J., Lam, B.Y., Larder, R., Tadross, J., Rimmington, D., Bosch, F., Cenzano, V.J., Ayuso, E., Ma, M.K., Rainbow, K. *et al.* (2018) Hypothalamic loss of Snord116 recapitulates the hyperphagia of Prader-Willi syndrome. *J. Clin. Invest.*, **128**, 960–969.
22. Bazeley, P.S., Shepelev, V., Talebizadeh, Z., Butler, M.G., Fedorova, L., Filatov, V. and Fedorov, A. (2008) snoTARGET shows that human orphan snoRNA targets locate close to alternative splice junctions. *Gene*, **408**, 172–179.
23. Bittel, D.C., Kibiryeva, N., McNulty, S.G., Driscoll, D.J., Butler, M.G. and White, R.A. (2007) Whole genome microarray analysis of gene expression in an imprinting center deletion mouse model of Prader-Willi syndrome. *Am. J. Med. Genet. A*, **143A**, 422–429.
24. Coulson, R.L., Powell, W.T., Yasui, D.H., Dileep, G., Resnick, J. and LaSalle, J.M. (2018) Prader-Willi locus Snord116 RNA processing requires an active endogenous allele and neuron-specific splicing by Rbfox3/NeuN. *Hum. Mol. Genet.*, **27**, 4051–4060.
25. Wu, H., Yin, Q.F., Luo, Z., Yao, R.W., Zheng, C.C., Zhang, J., Xiang, J.F., Yang, L. and Chen, L.L. (2016) Unusual processing generates SPA LncRNAs that sequester multiple RNA binding proteins. *Mol. Cell*, **64**, 534–548.
26. Yin, Q.F., Yang, L., Zhang, Y., Xiang, J.F., Wu, Y.W., Carmichael, G.G. and Chen, L.L. (2012) Long noncoding RNAs with snoRNA ends. *Mol. Cell*, **48**, 219–230.
27. Powell, W.T., Coulson, R.L., Crary, F.K., Wong, S.S., Ach, R.A., Tsang, P., Alice Yamada, N., Yasui, D.H. and Lasalle, J.M. (2013) A Prader-Willi locus lncRNA cloud modulates diurnal genes and energy expenditure. *Hum. Mol. Genet.*, **22**, 4318–4328.
28. Yugami, M., Kabe, Y., Yamaguchi, Y., Wada, T. and Handa, H. (2007) hnRNP-U enhances the expression of specific genes by stabilizing mRNA. *FEBS Lett.*, **581**, 1–7.
29. Chang, T.H., Huang, H.Y., Hsu, J.B., Weng, S.L., Horng, J.T. and Huang, H.D. (2013) An enhanced computational platform for investigating the roles of regulatory RNA and for identifying functional RNA motifs. *BMC Bioinformatics*, **14**, S4.
30. Agarwal, V., Bell, G.W., Nam, J.W. and Bartel, D.P. (2015) Predicting effective microRNA target sites in mammalian mRNAs. *Elife*, **4**, e05005. doi: 10.7554/eLife.05005.
31. Juzwik, C.A., Sienna, S.D., Zhang, Y., Paradis-Isler, N., Sylvester, A., Amar-Zifkin, A., Douglas, C., Morquette, B., Moore, C.S. and Fournier, A.E. (2019) microRNA dysregulation in neurodegenerative diseases: a systematic review. *Prog. Neurobiol.*, **182**, 101664. doi: 10.1016/j.pneurobio.2019.101664.
32. Wu, J., He, J., Tian, X., Luo, Y., Zhong, J., Zhang, H., Li, H., Cen, B., Jiang, T. and Sun, X. (2020) microRNA-9-5p alleviates blood-brain barrier damage and neuroinflammation after traumatic brain injury. *J. Neurochem.*, **153**, 710–726.
33. Hawley, Z.C.E., Campos-Melo, D. and Strong, M.J. (2019) MiR-105 and miR-9 regulate the mRNA stability of neuronal intermediate filaments. Implications for the pathogenesis of amyotrophic lateral sclerosis (ALS). *Brain Res.*, **1706**, 93–100.
34. Plass, M., Rasmussen, S.H. and Krogh, A. (2017) Highly accessible AU-rich regions in 3′ untranslated regions are hotspots for binding of regulatory factors. *PLoS Comput. Biol.*, **13**, e1005460. doi: 10.1371/journal.pcbi.1005460.
35. Zuccotti, P., Peroni, D., Potrich, V., Quattrone, A. and Dassi, E. (2020) Hyperconserved elements in human 5'UTRs shape essential post-transcriptional regulatory networks. *Front. Mol. Biosci.*, **7**, 220.
36. Chen, H., Victor, A.K., Klein, J., Tacer, K.F., Tai, D.J., de Esch, C., Nuttle, A., Temirov, J., Burnett, L.C., Rosenbaum, M. *et al.* (2020) Loss of MAGEL2 in Prader-Willi syndrome leads to decreased secretory granule and neuropeptide production. *JCI Insight*, **5**, e138576. doi: 10.1172/jci.insight.138576.
37. Good, D.J., Li, M. and Deater-Deckard, K. (2015) A genetic basis for motivated exercise. *Exerc. Sport Sci. Rev.*, **43**, 231–237.
38. Jiang, H. and Good, D.J. (2016) A molecular conundrum involving hypothalamic responses to and roles of long noncoding RNAs following food deprivation. *Mol. Cell. Endocrinol.*, **438**, 52–60.
39. Jiang, H., Modise, T., Helm, R., Jensen, R.V. and Good, D.J. (2015) Characterization of the hypothalamic transcriptome in response to food deprivation reveals global changes in long noncoding RNA, and cell cycle response genes. *Genes Nutr.*, **10**, 48.
40. Busch, A., Richter, A.S. and Backofen, R. (2008) IntaRNA: efficient prediction of bacterial sRNA targets incorporating target site accessibility and seed regions. *Bioinformatics*, **24**, 2849–2856.
41. Mann, M., Wright, P.R. and Backofen, R. (2017) IntaRNA 2.0: enhanced and customizable prediction of RNA-RNA interactions. *Nucleic Acids Res.*, **45**, W435–W439.
42. Raden, M., Ali, S.M., Alkhnbashi, O.S., Busch, A., Costa, F., Davis, J.A., Eggenhofer, F., Gelhausen, R., Georg, J., Heyne, S. *et al.* (2018) Freiburg RNA tools: a central online resource for RNA-focused research and teaching. *Nucleic Acids Res.*, **46**, W25–W29.
43. Wright, P.R., Georg, J., Mann, M., Sorescu, D.A., Richter, A.S., Lott, S., Kleinkauf, R., Hess, W.R. and Backofen, R. (2014) CopraRNA and IntaRNA: predicting small RNA targets, networks and interaction domains. *Nucleic Acids Res.*, **42**, W119–W123.
44. Lorenz, R., Bernhart, S.H., Höner zu Siederdissen, C., Tafer, H., Flamm, C., Stadler, P.F. and Hofacker, I.L. (2011) ViennaRNA package 2.0. *Algorithms Mol. Biol.*, **6**, 26. doi: 10.1186/1748-7188-6-26.